Numerical Investigation of Plant Tissue Porosity and its Influence on Cellular Level Shrinkage during Drying

H.C.P. Karunasena,[1,2] Y.T. Gu,[1] R.J. Brown[1] and W. Senadeera *[1]

Abstract

Dried plant food products are increasing in demand in the consumer market, leading to continuing research to develop better products and processing techniques. Plant materials are porous structures, which undergo large deformations during drying. For any given food material, porosity and other cellular parameters have a direct influence on the level of shrinkage and deformation characteristics during drying, which involve complex mechanisms. In order to better understand such mechanisms and their interrelationships, numerical modelling can be used as a tool. In contrast to conventional grid-based modelling techniques, it is considered that meshfree methods may have a higher potential for modelling large deformations of multiphase problem domains. This work uses a meshfree based microscale plant tissue drying model, which was recently developed by the authors. Here, the effects of porosity have been newly accounted for in the model with the objective of studying porosity development during drying and its influence on shrinkage at the cellular level. For simplicity, only open pores are modelled and in order to investigate the influence of different cellular parameters, both apple and grape tissues were used in the study. The simulation results indicated that the porosity negatively influences shrinkage during drying and the porosity decreases as the moisture content reduces (when open pores are considered). Also, there is a clear difference in the deformations of cells, tissues and pores, which is mainly influenced by the cell wall contraction effects during drying.

Keywords: Food drying; Porosity; Shrinkage; Plant tissue; Numerical modelling; Meshfree methods; SPH; DEM; Microscale models.

[1] *School of Chemistry, Physics and Mechanical Engineering, Faculty of Science and Engineering, Queensland University of Technology, 2-George Street, Brisbane,QLD 4001, Australia. Fax: +61 7 31381469; Tel: +61 7 31381009; E-mail:w3.senadeera@qut.edu.au (Wijitha Senadeera)*

[2] *Department of Mechanical and Manufacturing Engineering, Faculty of Engineering, University of Ruhuna, Hapugala, Galle, Sri Lanka. E-mail: chaminda@mme.ruh.ac.lk (H.C.P. Karunasena)*

1. Nomenclature

A	cell top surface area (m^2)
A_0	cell top surface area at fresh condition (m^2)
A/A_0	normalised cell area
A_c	total surface area of the cylindrical cell (m^2)
C	cell compactness
C_0	cell compactness at fresh condition
C/C_0	normalised cell compactness
D	cell Feret diameter (m)
D_{major}	cell major axis length (m)
D_{minor}	cell minor axis length (m)
D_0	cell Feret diameter at fresh condition (m)
D/D_0	normalised cell Feret diameter
E	Young's modulus of the cell wall material (MPa)
EL	cell elongation
EL_0	cell elongation at fresh condition
EL/EL_0	normalised cell elongation
$\boldsymbol{F}^e$	cell wall stiff forces (N)
$\boldsymbol{F}^d$	cell wall damping forces (N)
$\boldsymbol{F}^{rf}$	wall-fluid repulsion forces (N)
$\boldsymbol{F}^{rw}$	wall-wall repulsion forces (N)
$\boldsymbol{F}^a$	wall-fluid attraction forces (N)
$\boldsymbol{F}^b$	forces due to the bending stiffness of the wall (N)
$\boldsymbol{F}^p$	cell fluid pressure forces (N)
$\boldsymbol{F}^v$	cell fluid viscous forces (N)
G	shear modulus of the cell wall material (MPa)
K	cell fluid compression modulus (MPa)
L	width of a given discrete wall element (m)
L'	width of a given discrete wall element at fully turgid state (m)
L_0	initial width of a given discrete wall element (m)
L_p	cell wall permeability ($\text{m}^2\ \text{N}^{-1}\ \text{s}$)
P	cell perimeter (m)
P_0	cell perimeter at fresh condition (m)
P/P_0	normalised cell perimeter
P_a	pressure of any fluid particle a (Pa)
P_T	initial cell turgor pressure (Pa)
R	cell roundness

R_0	cell roundness at fresh condition
R/R_0	normalised cell roundness
S	ratio between fluid inter-particle distance and smoothing length (r_{ab}/h)
T	cell wall thickness (m)
T_0	initial cell wall thickness (m)
TP	positive cell turgor pressure effects
W	smoothing kernel
WD	cell wall contraction effects
WC	cell wall drying effects
X	x - coordinate axis
X	dry basis moisture content (kg $_{water}$/kg $_{dry\ solid}$)
X_0	dry basis moisture content at fresh condition
X/X_0	dry basis normalised moisture content
Y	y - coordinate axis
Z	cell height (m)
Z	z - coordinate axis
Z_0	initial cell height (m)
Z_t	cell height at the previous time step (m)
$Z_{t+\Delta t}$	cell height at the current time step (m)
f_0^{rf}	strength of the LJ repulsion forces between fluid and wall particles (N m^{-1})
f_0^{rw}	strength of the LJ repulsion forces between non-bonded wall particles (N m^{-1})
f_0^{a}	strength of the LJ attraction forces between fluid and wall particles (N m^{-1})
h	smoothing length (m)
h_0	initial smoothing length (m)
k_b	bending stiffness of cell wall material (N m rad^{-1})
k_{wc}	force coefficient of cell wall contractions (N m^{-1})
m_a	mass of any particle a (kg)
n_f	cell fluid particle number
n_w	cell wall particle number
r	cell radius (m)
r_{ab}	distance between any given particle a and b (m)
t	time (s)
$\boldsymbol{v}_{ab}$	velocity of any given particle a relative to any other particle b (m s^{-1})
$\boldsymbol{x}_{ab}$	position vector of any given particle a relative to any other particle b (m)
Δt	time step (s)
x_0	initial fluid grid spacing (m)
$\Delta\theta$	change of external angle θ of any given wall element (rad)
$\Delta\boldsymbol{x}_{ab}$	change of gap difference of any two particles a and b compared to their initial gap (m)
Π	osmotic potential of the cell (Pa)

α	factor governing the relationship between z-directional extension ratio and λ_θ of any wall element
β	parameter that relates 2-D deformations to 3-D deformations of any wall element
γ	cell wall damping constant (N m^{-1} s)
ε_0	initial minimum allowed gap between outermost fluid particles and cell wall particles (m)
θ	external angle between any adjacent cell wall elements (rad)
λ_θ	extension ratio of any given cell wall element
μ_a	dynamic viscosity of any fluid particle a (Pa s)
ρ_a	density of any given fluid particle a (kg m^{-3})
ρ_0	initial density of the cell fluid (kg m^{-3})
ρ_a^*	2-D density of any given particle a ($\rho_a^* = Z\rho_a$) (kg m^{-2})

2. Introduction

Food drying is a global industry providing a significant contribution to the food supply chain and economies. Among the different varieties of dried food products, plant-based products have a high popularity, mainly due to their natural source and balanced nutritional content. Since plant food materials contain a higher moisture content (usually about 90%), they are highly susceptible to microbial spoilage (Jangam, 2011). About 20% of the world's perishable crops are subjected to drying, mainly for preservation purposes (Grabowski, Marcotte, & Ramaswamy, 2003), with a variety of drying techniques being used (Martin, Osvaldo, Ganesan, Rakesh, & Weitnauer, 2006). Some of the critical phenomena that food structures can experience during drying include; shrinkage (Han, Yin, Li, Yang, & Ma, 2010; Hills & Remigereau, 1997; Lee, Salunkhe, & Nury, 1967; P.P. Lewicki & Drzewucka, 1998; Mayor, Silva, & Sereno, 2005; Ramos, Silva, Sereno, & Aguilera, 2004; Sabarez, Gallego-Juarez, & Riera, 2012; Witrowa-Rajchert & Rzạca, 2009) and porosity development (Karathanos, Kanellopoulos, & Belessiotis, 1996; Karunasena, Gu, Brown, & Senadeera, 2014; Sereno, Silva, & Mayor, 2007; Wang & Brennan, 1995; Zogzas, Maroulis, & Marinos-Kouris, 1994). Both these phenomena are highly interrelated (Madiouli, Sghaier, Lecomte, & Sammouda, 2012), with the final dried food characteristics being influenced significantly. Such phenomena are mainly influenced by the moisture content of the food material and drying temperature (Bai, Rahman, Perera, Smith, & Melton, 2002; Funebo, Ahrné, Kidman, Langton, & Skjöldebrand, 2000; Hills & Remigereau, 1997; Karunasena et al., 2014; P.P. Lewicki & Drzewucka, 1998; Piotr P. Lewicki & Pawlak, 2003; Mohammad Shafiur Rahman, Al-Zakwani, & Guizani, 2005; Sereno et al., 2007; Wang & Brennan, 1995; Zogzas et al., 1994). Also, there is a strong relationship between cellular level and bulk level changes (Karunasena et al., 2014a; Mayor & Sereno, 2004; Mayor et al., 2005; Ramos et al., 2004). In order to study these phenomena in detail, modelling is vital. In that regard, particularly for porosity development, both empirical (Karathanos et al., 1996; Karunasena et al., 2014; Sereno et

al., 2007; Wang & Brennan, 1995; Zogzas et al., 1994) and theoretical models (M. Shafiur Rahman, 2003) exist (M. Shafiur Rahman, 2001). Considering the various limitations of the empirical and theoretical models, numerical modelling can greatly assist in understanding the fundamental mechanisms involved. However, only a very limited number of such models are available, particularly for dried food structural deformations. These models are generally developed using grid-based modelling techniques such as finite element methods (FEM) and finite difference methods (FDM) (Fanta et al., 2014; Jeong, Park, & Kim, 2013; Z. Liu, Hong, Suo, Swaddiwudhipong, & Zhang, 2010). As a result, such techniques have limited capabilities to handle large deformations and phase change conditions of multiphasic non-continuum plant food materials (Karunasena, Senadeera, Brown, & Gu, 2014e).

As an alternative to such grid-based numerical modelling approaches, meshfree methods have recently gained much interest (Frank & Perré, 2010), mainly due to their fundamental capabilities of being able to account for large deformations of multiphasic non-continuum materials (G. R. Liu & Liu, 2003). Accordingly, based on a popular meshfree technique: smoothed particle hydrodynamics (SPH) and discrete element method (DEM), the authors have recently developed a modelling technique for microscale deformations of plant food materials during drying (Karunasena, Senadeera, Gu, & Brown, 2012c, 2012d, 2014b), highlighting the comparative advantage over the conventional grid-based modelling techniques. The technique was further developed into a comprehensive single cell drying model (Karunasena, Senadeera, Brown, & Gu, 2014c), and then further developed to tissue models (Karunasena et al., 2014e; Karunasena, Senadeera, Brown, & Gu, 2014f; Karunasena, Senadeera, Gu, & Brown, 2014d), even accounting for the characteristics of different plant materials (Karunasena, Brown, Gu, & Senadeera, 2015). Compared to conventional grid-based techniques, these models have a greater capability to account for the key cellular drying mechanisms such as cell moisture reduction, turgor loss, cell wall drying and wrinkling (Karunasena et al., 2015; Karunasena et al., 2014e).

However, in the above models, the main focus was to study the shrinkage of non-porous tissues. In order to better represent tissue shrinkage mechanisms during drying, it is important to also account for porosity, which is observed experimentally in plant tissues (Verboven et al., 2008). Therefore, this work is dedicated to numerically studying the influence of porosity on cellular shrinkage, and to investigate the trends of porosity development during drying. It should be noted here that although both the moisture content and the drying temperature are the key factors influencing porosity development, in this study, only the effect of moisture content variation is considered, in order to simplify the study. However, the meshfree based modelling technique used here can handle temperature dependent mechanisms, and this will be addressed by the authors in the future. Furthermore, porosity development and its influence on the shrinkage depend on the physical characteristics of the cellular structure of any given plant material. Therefore, in this study, two plant

materials (i.e. apple and grape) were simulated to show comparative differences. This work newly incorporates porosity to the meshfree-based tissue model recently developed by the authors (Karunasena et al., 2015; Karunasena et al., 2014e). Therefore, the main body of this article is more focused on the novel porosity implementation, rather than presenting the basic meshfree-based tissue model, which is summarised in Appendix A.

3. Model development

3.1. Modelling of plant tissues

The non-porous tissues were modelled by following the recent meshfree-based 2-D tissue modelling approach of the authors (Karunasena et al., 2015; Karunasena et al., 2014e). The model approximates a plant tissue to an aggregate of cylindrical individual cells as shown in Figure 1, where the fluid-dominated cell interior is modelled with SPH and the solid-dominated cell wall is modelled using the DEM. SPH was specifically used here for the fluid model considering the numerous advantages in the context of cell modelling, compared to the vertex models and gel-material models that are also available in the literature (Karunasena et al., 2014c). For simplicity, cellular mechanisms and deformations are studied in 2-D by referring to the top surface of each cell of the tissue, assuming uniform axial cell deformations. The cell wall is approximated to a circular boundary made out of a visco-elastic solid material and modelled using DEM, assuming a neo-Hookean solid material model along with a supplementary viscous term (Liedekerke et al., 2010; Van Liedekerke et al., 2011). Accordingly, Figure 2 and Figure 3 present the distinct force interactions used to define the cell wall, and the cell fluid mechanisms and interactions (Karunasena et al., 2014e) (see Section 8.1 and 8.2 of Appendix A for details). Then, as shown in Figure 4, such cells are initiated as hexagons and aggregated to form a basic honeycomb-shaped cellular structure, frequently observed in real plant tissues (Karunasena et al., 2014e) (see Section 8.3 of Appendix A for details).

In order to study the influence of different cellular properties on porosity and shrinkage characteristics during drying, both apple and grape tissues were modelled and compared with the use of a simplified square-shaped tissue structure, consisting of 39 aggregated cells. This limited number of cells had to be selected mainly due to concerns over computational costs. The two particular plant materials were selected by considering the industrial importance and the comparable structural and physical characteristics at the cellular level. Prior to any simulations, tissues were set up by placing cell wall and fluid particles of each cell in a honeycomb structure such that the inter-particle spacing is the same (Karunasena et al., 2015). Considering the model consistency and computational cost, a moderately-high particle resolution was used by involving 96 wall particles and 656 fluid particles (Karunasena et al., 2014e; Karunasena et al., 2014b). Table 1 gives the customised physical

properties used for each of the plant material, and Table 2 presents the other model parameters commonly used for modelling.

3.2. Simulation of plant tissue porosity and shrinkage during drying

For non-porous tissue simulations, the above mentioned square tissue of 39 cells was used without any alterations. For porous tissue simulations, different porosity values were achieved by removing the interior cells of the tissue. Accordingly, tissues with 5, 10, 15 and 20 % porosity (approximately), were obtained by removing 2, 4, 6 and 7 interior cells from the original 39-cell tissue, as presented in Fig 5(a). The cells were removed such that, each pore is connected to the tissue by all its sides. The effect of connected pores was not considered in this study due to the limited size of the tissue involved. Further, it should be noted that the pores used for the simulations are open pores, which are assumed to be connected with the atmosphere from the top and bottom surfaces of each tissue (See Figure 1(a)). Also, case-hardening effects were not considered here and all the cells in the tissue were assumed to undergo a uniform drying process. Accordingly, tissues were time evolved following the method described in one of the recent works of authors (Karunasena et al., 2015) (see Section 8.4 in Appendix A).

3.3. Computational implementation and model consistency

Both the non-porous and porous tissue models were set up as parallel C++ computer programs. High Performance Computing (HPC) facility of Queensland University of Technology (QUT), Australia was used to perform the simulations. The HPC facility was such that Xeon E5-2670 nodes of 6 cores were used for each simulation where each core was having 2.66 GHz processor and 256 GB RAM. The commonly used Leapfrog time integrator (G. R. Liu & Liu, 2003) was used for time evolution with a sufficiently small time step in order to ensure model stability, which is defined by the Courant-Friedrichs-Lewy (CFL) criteria (Colagrossi, Bouscasse, Antuono, & Marrone, 2012; G. R. Liu & Liu, 2003). The C++ source code was developed by referring to an existing Fortran-based SPH source code (G. R. Liu & Liu, 2003). Open visualization tool (OVITO) (Stukowski, 2010) was used for model visualisations. The computational accuracy of the model was evaluated using a consistency error parameter (Karunasena et al., 2014b), and it was found that the model consistency error was maintained within ±3 %.

3.4. Use of experimental literature for model development and validation

As mentioned in Section 2.1, the majority of the key physical properties used for modelling the two tissue types were directly adopted from experimental literature (Karunasena et al., 2015). Also, for the qualitative and quantitative comparison of the model predictions, experimental literature on dried apple and grape tissues was used according to Table 3.

4. Results and discussion

4.1. Study of apple tissue shrinkage as influenced by porosity

Figure 5 presents the initial states (before simulations) and final states (after simulations), of non-porous and porous apple tissue models. In the case of non-porous tissues, it is evident that compared to the initial state, the fresh tissue has inflated and settled to a cellular arrangement resembling a turgid cell structure, commonly observed in fresh plant tissues. The cell walls are highly stretched and the turgor pressure reaches a maximum in this case (according to Table 2, fresh cell turgor pressure will be around 200 kPa; see Section 8.4 in Appendix A for details). Then, as the drying begins and progresses, moisture content levels gradually reduce, the tissue undergoes gradual shrinkage and deformations occurs in both cellular and tissue scales, with the presence of cell wall wrinkling and turgor loss (Karunasena et al., 2014e). Furthermore, as the moisture content reduces, the dried cells gradually lose their initial turgid nature and the sizes become smaller, and shapes become altered. This compares well with the experimentally observed dried tissue deformations as presented in Figure 6. The SEM images of apple cells and tissues indicate that their sizes and their shapes largely vary with the influence of drying. Wrinkling of the cell walls and cellular shrinkage are clearly observed. However, from the SEM images, the cells and pores are somewhat difficult to distinguish, which is a limitation of the particular experimental technique used (Karunasena et al., 2014a).

When referring to the porous tissue simulation results presented in Figure 5, it is evident that the pores also undergo shrinkage during drying, quite similar to that of cells, which has also been reported in experimental literature (P.P. Lewicki & Drzewucka, 1998; Piotr P. Lewicki & Pawlak, 2003; Mayor et al., 2005). However, it should be noted here that the locked-in pores of the cellular structure can undergo expansions during drying (Lozano, Rotstein, & Urbicain, 1980). This is particularly evident at higher temperatures in the final stages of drying, due to expansion of the gaseous constituents (Hills & Remigereau, 1997; Mohammad Shafi ur, 2008; Mohammad Shafiur Rahman et al., 2005). Since the pores used for these simulations are open pores (see Section 2.2), and no specific material models were involved to model the mechanisms of the pores, such expansions of the pores during drying are unexpected. However, one can develop such models by incorporating gaseous materials inside pores and even incorporating temperature influences for their expansion, but these were not considered here. It was observed that the shrinkage of porous tissues was lower, compared to the non-porous tissue, which is due to the absence of the full array of shrinking cells, inside the tissue. This can be clearly observed when comparing Fig 5(f) corresponding to non-porous tissue and the porous tissues. Also, even the higher-porous tissues (20 % or 15 %) have undergone limited shrinkage compared to lower-porous tissues (10 % or 5 %). In addition, the shrinkage of pores becomes limited as the tissue porosity increases. This is evident when comparing the pore sizes of tissues, particularly in Figure 5(f). The main cause of this behaviour is the existence of loose contacts between cells as well as the

8

absence of interior cells that largely shrink during dying, influencing the shrinkage of open pores. To elaborate these shrinkage differences further, quantitative results obtained for these simulations are presented next and are compared with experimental findings.

The quantitative study is based on several cellular geometric parameters: cell area (A), Feret diameter[3] (D), perimeter (P), roundness[4] (R), elongation[5] (EL) and compactness[6] (C) (Karunasena et al., 2014a). The normalised parameters are finally calculated and used for the analysis (X/X_0, A/A_0, D/D_0, P/P_0, R/R_0, EL/EL_0 and C/C_0), which assists comparison and easy identification of the trends. From the results presented in Figure 7, the experimental curves indicate reducing trends of cell area, Feret diameter and perimeter which correspond to the gradual shrinkage of the apple cells and tissues during drying. Further, localised in-homogeneous shape changes of the cells are represented by the reducing trends of the roundness and the compactness, and the increasing trends of the elongation (Karunasena et al., 2014a). It was observed that there is acceptable agreement between the experimental findings and the model predictions, implying that the meshfree-based modelling approach is sufficiently capable of modelling cellular shrinkage during drying. Furthermore, porous tissues indicated a far better agreement with the experimental curves, implying that the porosity is an important mechanism to be incorporated in numerical modelling of plant tissues during drying. Particularly the curves of A, D, R, EL and C indicated that pores reduced the over-prediction of the corresponding shrinkage trends of the models. However, the perimeter variation was not influenced by the porosity, which is expected, since it is mainly due to internal cell mechanisms rather than due to the external influences such as pores, which basically influence only the shape changes of cells. It was further evident that different porosity levels have not indicated much of deviations of the trends, which should be mainly caused by the limitation of this model, since only open pores were considered while omitting locked-in pores. Also, another limitation of the tissue model used here is its single-layered structure (see Figure 1(a)). On the other hand, the tissues used for microscopic examinations were of finite dimensions and involved complex multi-layered 3-D cellular and tissue mechanisms. Further, particularly for apple tissue drying, it should be noted that, even though the experimental results were obtained until the samples were well dried where they reach about 0.01 X/X_0 (Karunasena et al., 2014a), due to numerical instability of the tissue model at extremely dried conditions, simulations were only possible until 0.3 X/X_0. However, this is a significant achievement in terms of numerical modelling when compared with the state of the art FEM based tissue drying models available in literature, which can only simulate deformations of tissues until 0.7 X/X_0 (Fanta et al., 2014).

---

[3] $\sqrt{4A/\pi}$
[4] $4\pi A/P^2$
[5] $\sqrt{4A/\pi}$ /(major axis length)
[6] major axis length/minor axis length

4.2. Study of grape tissue shrinkage as influenced by porosity

In order to study the influences of the cellular physical properties for shrinkage during drying, grape tissues were also modelled and the results are presented in Figure 8. Here also, it is observed that the pores tend to limit the tissue shrinkage, and in the meantime pores also undergo shrinkage during drying. Furthermore, as observed in apple tissues, the shrinkage of pores is limited in highly porous tissues. These trends can be explained in a similar manner to that of apple tissues as presented in Section 3.1. However, compared to the apple tissues, the shrinkage of grape cells, tissues and pores is higher, which is due to the differences in the physical properties of the two plant materials. According to Table 1, the main cause for this trend is the higher cell wall contraction effects of the grape cells. The cell wall contraction force field is defined in Eq. A.8, where a higher a/b ratio will lead to increased cell wall contraction forces, leading to a high level of cellular shrinkage. Since pores are well attached to the cells, they undergo higher shrinkage as a result of the higher cellular shrinkage. However, Table 1 provides clues for the non-significant influence of the cell wall stiffness for these differences of the shrinkage trends. It is because, although the grape cell walls are of half the thickness of that of the apple cells, the cell wall stiffness of grape cells will be quite similar to that of apple cells, since the cell wall shear modulus of the grape is set as three times higher than that of apple cells (see Table 1 and Eq. A.2 in Section 8.1). Furthermore, Figure 9 presents stereo microscopy images of fresh and dried grape tissues, which basically represents the first stage of drying where the moisture content reduction is limited to 0.6 X/X_0 (Ramos et al., 2004). Here, compared to the turgid fresh cells, the dried cells have undergone some degree of shrinkage and cell wall wrinkling, which basically agrees with the simulation results discussed above. However, due to the lower magnification used for imaging, no further qualitative details are evident from the images. The paragraph below presents the quantitative results corresponding to the shrinkage of different porous tissues.

With respect to the above mentioned geometric parameters, Figure 10 compares the model predictions, along with a set of experimental results obtained from literature (Ramos, 2010; Ramos et al., 2004). The overall observation is that the porous tissues undergo limited shrinkage compared to the dense tissues, providing a good agreement with the qualitative simulation results presented above. This trend is clearly observed from the graphs corresponding to A, D, R, EL and C. Here also, the cell perimeter was minimally influenced by porosity, which could be due to the cell wall contractions forces, as explained above. The overall close agreement between the numerical results and the experimental findings indicates that the meshfree modelling approach is flexible enough to model different tissue types and their related cellular mechanisms. Also, since a favourable agreement is observed from the model predictions and the experimental findings, the modelling approach can be considered as having sufficient capability to model cellular deformations of plant materials during drying.

4.3. Comparative differences of shrinkage of apple and grape tissues

In order to study the comparative differences between shrinkage behaviours of apple and grape cellular structures during drying, with the presence of porosity, the extremely dry tissue states of the above simulation results are shown in Figure 11, with a higher magnification. When considering the dense tissues, grape tissue undergoes higher shrinkage with clearly identifiable cell wall wrinkling effects. It was further observed that cell wall wrinkling was significant towards the centre of the tissue, which could be due to the larger number of neighbouring cells, which are subject to higher geometrical contractions. Also, when considering the porous tissues, it was clearly observed that the pores of grape tissues were smaller compared to the apple pores, and the sides of the pores had smaller radii of curvature. These findings imply that geometry of the dried cellular structure and the deformations of cells, tissues and pores are also largely influenced by the physical properties and characteristics of the cellular structure.

4.4. Study of porosity development during drying

For both apple and grape tissues, the development of porosity during drying was studied quantitatively by observing changes of the normalised porosity values as presented in Figure 12. It can be observed from Figures 12(a) and (b) that predicted porosity decreased during drying, which is mainly due to the limitation of this model, since only the open pores were considered. However, in reality during tissue drying, locked-in pores tend to expand, leading to an increase in porosity (Karathanos et al., 1996; Karunasena et al., 2014; Sereno et al., 2007; Wang & Brennan, 1995; Zogzas et al., 1994). Furthermore, both tissue simulation results imply that the low-porous tissues undergo comparatively severe porosity decrements compared to high-porous tissues. The trends for normalised porosity indicate that grape tissues have higher variations of porosity compared to the apple tissues, which should be due to the higher cell wall contraction effects, discussed above. It should be noted that, although the model does not account for the gaseous constituents of the pores and the mechanisms leading to expansions, the numerical modelling results still provide some useful comparative insights on how different tissues can behave under different drying conditions, as a result of differences in their physical characteristics.

In Figure 12, the porosity variation of both apple and grape showed some fluctuations, which were mainly due to the nonlinear and localised deformation characteristics of the cellular structure during drying, which is even evident from both experimental results and the simulations presented in Figure 7 and Figure 10. Those fluctuations were also influenced by the variation of the numerical consistency error of each individual cell in the tissue model (Karunasena et al., 2014b), when the shapes of the cells become irregular corresponding to different states of dryness and locations of the cells within the tissues. Furthermore, it should be noted that there can be variations in the pectin layer properties during drying, which has not yet been experimentally studied in great detail as per the available

literature. Due to such limitations, in this study, the pectin layer properties were assumed to be consistent throughout the drying process. However, the model used in this work also has the potential to incorporate such variations.

5. Conclusion and outlook

The main focus of this study was to numerically investigate the behaviour of plant tissue shrinkage during drying as influenced by porosity. A series of simulations were conducted by using a 2-D meshfree-based plant tissue model recently developed by the authors. In order to further study the influence of porosity on different tissue types, apple and grape tissues were modelled. In each case, both non-porous and porous tissues (5, 10, 15 and 20% porous) were modelled, and the results were compared with experimental data from the literature. For this study, only open pores were considered and therefore locked-in pores and the expandability of their gaseous constituents were omitted. The main conclusions of the study are:

- Porosity of the tissue resists shrinkage, leading to limited overall tissue deformations and localised cellular deformations.
- Pores in tissues are subject to shrinkage, similar to the cells in the tissue.
- Compared to the low-porous tissues, pores in high-porous tissues undergo limited shrinkage.
- During drying, cells and pores in grape tissues are subject to higher shrinkage, compared to apple tissues. Cell wall wrinkling can be clearly observed in grape tissues. This overall behaviour is mainly due to the intense cell wall contraction effects of grape cells.
- When only open pores are present in the tissue, the porosity reduces during drying, which is not the case if locked-in pores are present, which undergo expansions during drying, leading to increased porosity (as observed in the experiments).
- Quantitative results, involving cellular geometric parameters indicated a gradual shrinking behaviour of both the plant materials. Particularly, in the case of apple tissue, the tissue models with porosity favourably agree with the experimental curves, implying the existence of pores in real tissues.
- Model predictions indicated an acceptable agreement with experimental findings in most of the instances, implying the potential application of the meshfree based modelling technique to model plant tissue morphological changes during drying.

Furthermore, one can develop more advanced porous tissue models by incorporating gaseous pore constituents and their physical mechanisms, in order to account for critical phenomena such as pore expansion during drying, which is observed in actual experiments. Also, the influence of temperature for porosity development can be studied, which is highly related to industrial drying applications. One could even further develop the existing model into a 3-D tissue model and incorporate multiscale

techniques to develop bulk-scale models. Since the meshfree based technique used for this study is fundamentally capable of incorporating such developments, this modelling work has a high potential for further developments.

6. Acknowledgements

7. References

Bai, Y., Rahman, M. S., Perera, C. O., Smith, B., & Melton, L. D. (2002). Structural Changes in Apple Rings during Convection Air-Drying with Controlled Temperature and Humidity. *Journal of Agricultural and Food Chemistry, 50*(11), 3179-3185. doi: 10.1021/jf011354s

Colagrossi, A., Bouscasse, B., Antuono, M., & Marrone, S. (2012). Particle packing algorithm for SPH schemes. *Computer Physics Communications, 183*(8), 1641-1653. doi: http://dx.doi.org/10.1016/j.cpc.2012.02.032

Fanta, S. W., Abera, M. K., Aregawi, W. A., Ho, Q. T., Verboven, P., Carmeliet, J., & Nicolai, B. M. (2014). Microscale modeling of coupled water transport and mechanical deformation of fruit tissue during dehydration. *Journal of Food Engineering, 124*(0), 86-96. doi: http://dx.doi.org/10.1016/j.jfoodeng.2013.10.007

Frank, X., & Perré, P. (2010). The Potential of Meshless Methods to Address Physical and Mechanical Phenomena Involved during Drying at the Pore Level. *Drying Technology, 28*(8), 932-943. doi: 10.1080/07373937.2010.497077

Funebo, T., Ahrné, L. l. a., Kidman, S., Langton, M., & Skjöldebrand, C. (2000). Microwave heat treatment of apple before air dehydration – effects on physical properties and microstructure. *Journal of Food Engineering, 46*(3), 173-182. doi: 10.1016/s0260-8774(00)00080-7

Grabowski, S., Marcotte, M., & Ramaswamy, H. S. (2003). Drying of Fruits, Vegetables, and Spices In A. Chakraverty, A. S. Mujumdar, G. S. V. Raghavan & H. Rawaswamy (Eds.), *Handbook of postharvest technology : cereals, fruits, vegetables, tea, and spices* (pp. 653-695). New York Marcel Dekker.

Han, Q.-H., Yin, L.-J., Li, S.-J., Yang, B.-N., & Ma, J.-W. (2010). Optimization of Process Parameters for Microwave Vacuum Drying of Apple Slices Using Response Surface Method. *Drying Technology, 28*(4), 523-532. doi: 10.1080/07373931003618790

Hills, B. P., & Remigereau, B. (1997). NMR studies of changes in subcellular water compartmentation in parenchyma apple tissue during drying and freezing. *International Journal of Food Science & Technology, 32*(1), 51-61. doi: 10.1046/j.1365-2621.1997.00381.x

Jangam, S. V. (2011). An Overview of Recent Developments and Some R&D Challenges Related to Drying of Foods. *Drying Technology, 29*(12), 1343-1357. doi: 10.1080/07373937.2011.594378

Jeong, S., Park, S.-H., & Kim, C.-H. (2013). Simulation of Morphology Changes in Drying Leaves. *Computer Graphics Forum, 32*(1), 204-215. doi: 10.1111/cgf.12009

Karathanos, V. T., Kanellopoulos, N. K., & Belessiotis, V. G. (1996). Development of porous structure during air drying of agricultural plant products. *Journal of Food Engineering, 29*(2), 167-183. doi: 10.1016/0260-8774(95)00058-5

Karunasena, H. C. P., Brown, R. J., Gu, Y. T., & Senadeera, W. (2015). Application of meshfree methods to numerically simulate microscale deformations of different plant food materials during drying. *Journal of Food Engineering, 146*(0), 209-226. doi: http://dx.doi.org/10.1016/j.jfoodeng.2014.09.011

Karunasena, H. C. P., Gu, Y. T., Brown, R. J., & Senadeera, W. (2014). Numerical Investigation of Case Hardening of Plant Tissue during Drying and Its Influence on the Cellular Level Shrinkage. *Drying Technology*, null-null. doi: 10.1080/07373937.2014.982759

Karunasena, H. C. P., Hesami, P., Senadeera, W., Gu, Y. T., Brown, R. J., & Oloyede, A. (2014a). Scanning Electron Microscopic Study of Microstructure of Gala Apples During Hot Air Drying. *Drying Technology, 32*(4), 455-468. doi: http://dx.doi.org/10.1080/07373937.2013.837479

Karunasena, H. C. P., Senadeera, W., Brown, R. J., & Gu, Y. T. (2014c). Simulation of plant cell shrinkage during drying – A SPH–DEM approach. *Engineering Analysis with Boundary Elements, 44*(0), 1-18. doi: http://dx.doi.org/10.1016/j.enganabound.2014.04.004

Karunasena, H. C. P., Senadeera, W., Brown, R. J., & Gu, Y. T. (2014e). A Particle Based Model to Simulate Microscale Morphological Changes of Plant Tissues during Drying. *Soft Matter, 10*(29), 5249-5268. doi: http://dx.doi.org/10.1039/C4SM00526K

Karunasena, H. C. P., Senadeera, W., Brown, R. J., & Gu, Y. T. (2014f). *A Novel Approach for Numerical Simulation of Plant Tissue Shrinkage During Drying*. Paper presented at the International Research Symposium on Postharvest Technology, Anuradapura, Sri Lanka. http://www.ipht.lk/Pro%20section%2004.pdf

Karunasena, H. C. P., Senadeera, W., Gu, Y. T., & Brown, R. J. (2012c, 25-28 November 2012). *A particle based micromechanics model to simulate drying behaviors of vegetable cells*. Paper presented at the 4th International Conference on Computational Methods (ICCM 2012), Gold Coast, Australia.

Karunasena, H. C. P., Senadeera, W., Gu, Y. T., & Brown, R. J. (2012d, 3-7 December 2012). *A Coupled SPH-DEM Model for Fluid and Solid Mechanics of Apple Parenchyma Cells During Drying*. Paper presented at the 18th Australian Fluid Mechanics Conference, Launceston - Australia.

Karunasena, H. C. P., Senadeera, W., Gu, Y. T., & Brown, R. J. (2014b). A Coupled SPH-DEM Model for Micro-scale Structural Deformations of Plant Cells during Drying. *Applied Mathematical Modelling, 38*(15-16), 3781-3801. doi: http://dx.doi.org/10.1016/j.apm.2013.12.004

Karunasena, H. C. P., Senadeera, W., Gu, Y. T., & Brown, R. J. (2014d). A Meshfree Model for Plant Tissue Deformations during Drying. *ANZIAM Journal, 55 (EMAC2013)*, C110-C137.

Lee, C. Y., Salunkhe, D. K., & Nury, F. S. (1967). Some chemical and histological changes in dehydrated apple. *Journal of the Science of Food and Agriculture, 18*(3), 89-93. doi: 10.1002/jsfa.2740180302

Lewicki, P. P., & Drzewucka, J. (1998). *Effect of drying on tissue structure of selected fruits and vegetables*. Paper presented at the Proceedings of the 11th International Drying Symposium Drying 98, Greece.

Lewicki, P. P., & Pawlak, G. (2003). Effect of Drying on Microstructure of Plant Tissue. *Drying Technology, 21*(4), 657-683. doi: 10.1081/drt-120019057

Liedekerke, P. V., Ghysels, P., Tijskens, E., Samaey, G., Smeedts, B., Roose, D., & Ramon, H. (2010). A particle-based model to simulate the micromechanics of single-plant parenchyma cells and aggregates. *Physical Biology, 7*(2), 026006.

Liu, G. R., & Liu, M. B. (2003). *Smoothed Particle Hydrodynamics : A Meshfree Particle Method*. Singapore: World Scientific Publishing Co.

Liu, Z., Hong, W., Suo, Z., Swaddiwudhipong, S., & Zhang, Y. (2010). Modeling and simulation of buckling of polymeric membrane thin film gel. *Computational Materials Science, 49*(1, Supplement), S60-S64. doi: http://dx.doi.org/10.1016/j.commatsci.2009.12.036

Lozano, J. E., Rotstein, E., & Urbicain, M. J. (1980). Total porosity and open-pore porosity in the drying of fruits. *Journal of Food Science, 45*(5), 1403-1407. doi: 10.1111/j.1365-2621.1980.tb06564.x

Madiouli, J., Sghaier, J., Lecomte, D., & Sammouda, H. (2012). Determination of porosity change from shrinkage curves during drying of food material. *Food and Bioproducts Processing, 90*(1), 43-51. doi: http://dx.doi.org/10.1016/j.fbp.2010.12.002

Martin, O., Osvaldo, C., Ganesan, N., Rakesh, S., & Weitnauer, A. (2006). Food Dehydration. In R. H. Dennis & D. B. Lund (Eds.), *Handbook of Food Engineering, Second Edition* (pp. 601-744): CRC Press.

Mayor, L., & Sereno, A. M. (2004). Modelling shrinkage during convective drying of food materials: a review. *Journal of Food Engineering, 61*(3), 373-386. doi: 10.1016/s0260-8774(03)00144-4

Mayor, L., Silva, M. A., & Sereno, A. M. (2005). Microstructural Changes during Drying of Apple Slices. *Drying Technology, 23*(9-11), 2261-2276. doi: 10.1080/07373930500212776

Mohammad Shafi ur, R. (2008). Dehydration and Microstructure *Advances in Food Dehydration* (pp. 97-122): CRC Press.

Rahman, M. S. (2001). Toward prediction of porosity in foods during drying: a brief review. *Drying Technology, 19*(1), 1-13. doi: 10.1081/drt-100001349

Rahman, M. S. (2003). A Theoretical Model to Predict the Formation of Pores in Foods During Drying. *International Journal of Food Properties, 6*(1), 61-72. doi: 10.1081/jfp-120016624

Rahman, M. S., Al-Zakwani, I., & Guizani, N. (2005). Pore formation in apple during air-drying as a function of temperature: porosity and pore-size distribution. *Journal of the Science of Food and Agriculture, 85*(6), 979-989. doi: 10.1002/jsfa.2056

Ramos, I. N. (2010). *Integrated Approach on Field Solar Drying, Pilot Convective Drying and Microstructural Changes.* (PhD (Food Science and Technology)), Catholic University of Portugal Porto - Portugal.

Ramos, I. N., Silva, C. L. M., Sereno, A. M., & Aguilera, J. M. (2004). Quantification of microstructural changes during first stage air drying of grape tissue. *Journal of Food Engineering, 62*(2), 159-164. doi: 10.1016/s0260-8774(03)00227-9

Sabarez, H. T., Gallego-Juarez, J. A., & Riera, E. (2012). Ultrasonic-Assisted Convective Drying of Apple Slices. *Drying Technology, 30*(9), 989-997. doi: 10.1080/07373937.2012.677083

Schlosser, J., Olsson, N., Weis, M., Reid, K., Peng, F., Lund, S., & Bowen, P. (2008). Cellular expansion and gene expression in the developing grape (Vitis vinifera L.). *Protoplasma, 232*(3-4), 255-265. doi: 10.1007/s00709-008-0280-9

Sereno, A. M., Silva, M. A., & Mayor, L. (2007). Determination of Particle Density and Porosity in Foods and Porous Materials with High Moisture Content. *International Journal of Food Properties, 10*(3), 455-469. doi: 10.1080/10942910600880736

Stukowski, A. (2010). Visualization and analysis of atomistic simulation data with OVITO–the Open Visualization Tool. *Modelling and Simulation in Materials Science and Engineering, 18*(1), 015012.

Taiz, L., & Zeiger, E. (2010). Water and Plant Cells *Plant Physiology* (pp. 73-84): Sinauer Associates, Sunderland, USA.

Van Liedekerke, P., Ghysels, P., Tijskens, E., Samaey, G., Roose, D., & Ramon, H. (2011). Mechanisms of soft cellular tissue bruising. A particle based simulation approach. *Soft Matter, 7*(7), 3580-3591.

Verboven, P., Kerckhofs, G., Mebatsion, H. K., Ho, Q. T., Temst, K., Wevers, M., . . . Nicolaï, B. M. (2008). Three-Dimensional Gas Exchange Pathways in Pome Fruit Characterized by Synchrotron X-Ray Computed Tomography. *Plant Physiology, 147*(2), 518-527.

Wang, N., & Brennan, J. G. (1995). Changes in structure, density and porosity of potato during dehydration. *Journal of Food Engineering, 24*(1), 61-76. doi: 10.1016/0260-8774(94)p1608-z

Witrowa-Rajchert, D., & Rząca, M. (2009). Effect of Drying Method on the Microstructure and Physical Properties of Dried Apples. *Drying Technology, 27*(7-8), 903-909. doi: 10.1080/07373930903017376

Wu, N., & Pitts, M. J. (1999). Development and validation of a finite element model of an apple fruit cell. *Postharvest Biology and Technology, 16*(1), 1-8. doi: 10.1016/s0925-5214(98)00095-7

Zogzas, N. P., Maroulis, Z. B., & Marinos-Kouris, D. (1994). Densities, Shrinkage and Porosity of Some Vegetables during Air Drying. *Drying Technology, 12*(7), 1653-1666. doi: 10.1080/07373939408962191
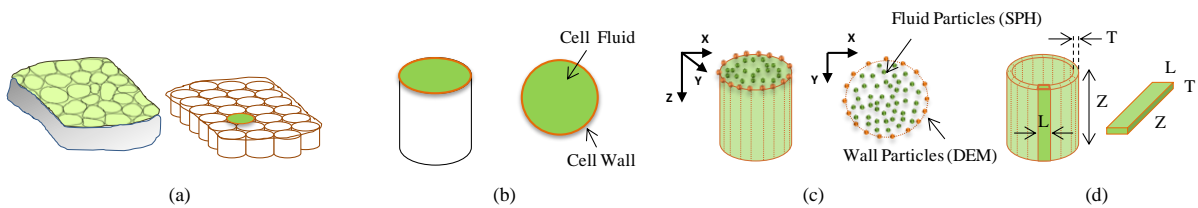
8. Figures and tables

Fig. 1. (a) A plant tissue simply represented as an aggregate of cylindrical cells, (b) 2-D model to represent any cylindrical cell; (c) particle scheme used for the 2-D Cell model: fluid model based on SPH particles and wall model based on DEM particles; and (d) discrete elements of the cell wall.
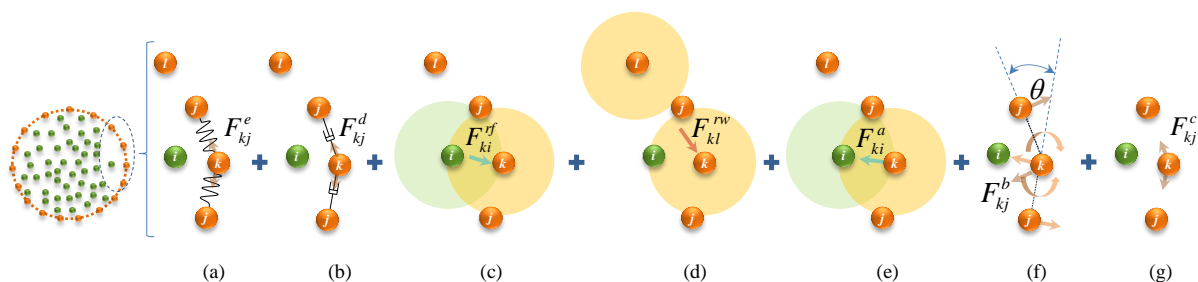

Fig. 2. Force interactions used in the DEM-based cell wall model: wall stiff forces (F_{kj}^e), wall damping forces (F_{kj}^d), wall-fluid repulsion forces (F_{ki}^{rf}), non-bonded wall-wall repulsion forces (F_{kl}^{rw}), wall-fluid attraction forces (F_{ki}^a), forces due to wall bending stiffness (F_{kj}^b), and forces for cell wall contractions during drying (F_{kj}^c). (i : fluid particles; j, k & l : wall particles)
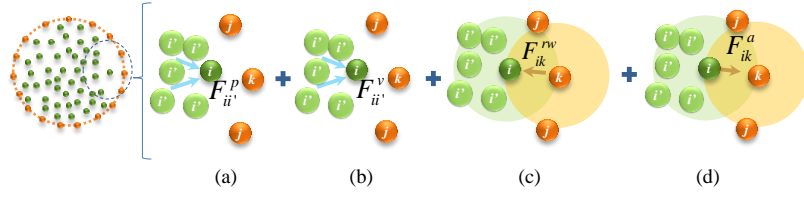
Fig. 3. Force interactions used in the SPH-based cell fluid model: pressure force ($\boldsymbol{F}_{ii'}^{p}$), viscous force ($\boldsymbol{F}_{ii'}^{v}$), wall-fluid repulsion forces ($\boldsymbol{F}_{ik}^{rw}$), and wall-fluid attraction forces ($\boldsymbol{F}_{ik}^{a}$). (i & i' : fluid particles; j & k: wall particles)
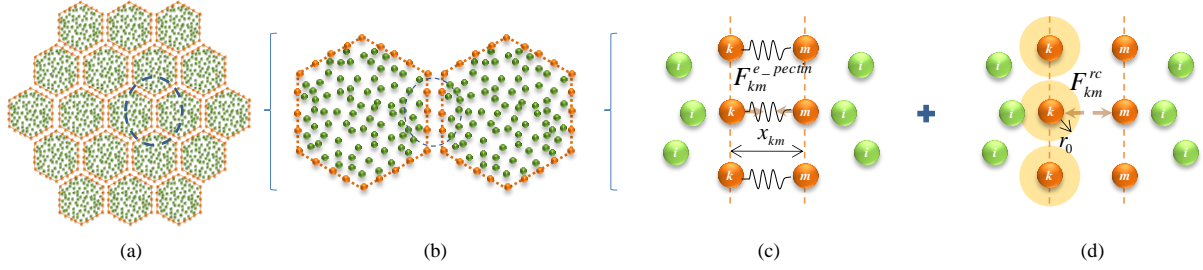

Fig. 4. Tissue model and cell-cell force interactions: (a) hexagonal shaped cells are used for tissue initialisation with positive pectin layer gap; (b) interacting wall particle pairs of adjacent cells; (c) pectin layer stiff forces ($\boldsymbol{F}_{km}^{e\_pectin}$); and (d) cell-cell repulsion forces ($\boldsymbol{F}_{km}^{rc}$). (i: fluid particles; k & m: wall particles)

Table 1 Customised model parameters for different plant materials

Parameter	Food variety used for modelling	
	Apple	Grape
	Value (Source)	Value (Source)
Initial cell diameter (D_0)	150 μm (Karunasena et al., 2014a)	150 μm (Schlosser et al., 2008)
Initial cell height (Z_0)	100 μm ($= 2/3\ D_0$)	100 μm ($= 2/3\ D_0$)
Wall initial thickness (T_0)	6 μm (Liedekerke et al., 2010; Wu & Pitts, 1999)	3 μm (Schlosser et al., 2008)
Pectin layer thickness (T_p)	8 μm (Karunasena et al., 2015)	8 μm (Karunasena et al., 2015)
Pectin layer stiffness (k_{pectin})	20 N m^{-1} (Karunasena et al., 2015)	20 N m^{-1} (Karunasena et al., 2015)
Wall shear modulus (G) $\approx E/3$	18 MPa (Liedekerke et al., 2010; Wu & Pitts, 1999)	33 MPa (Karunasena et al., 2015)
Empirical factors on cell wall contraction (a, b)	0.2, 0.9 (Karunasena et al., 2014a)	0.18, 0.43 (Ramos, 2010)
Fresh cell turgor pressure (P_T)	200 kPa (Liedekerke et al., 2010)	200 kPa (Karunasena et al., 2015)
Fresh cell osmotic potential (Π)	-200 kPa ($= -P_T$)	-200 kPa ($= -P_T$)

Table 2 Commonly used model parameters for all plant materials

Parameter	Value	Source
Fluid viscosity (μ)	0.1 Pa s	set (Liedekerke et al., 2010)
Initial fluid density (ρ_0)	1000 kg m^{-3}	set (Liedekerke et al., 2010)
Wall permeability (L_P)	2.5×10^{-6} m^2 N^{-1} s	set (Karunasena et al., 2014b)
Wall bending stiffness (k_b)	1×10^{-12} N m rad^{-1}	set (Karunasena et al., 2014e)
Wall damping ratio (γ)	5×10^{-6} N m^{-1} s	set (Karunasena et al., 2014b)
Fluid compression modulus (K)	20 MPa	set (Karunasena et al., 2014b)
Wall contraction force coefficient (k_{wc})	4×10^{4} N m^{-1}	set (Karunasena et al., 2014e)
LJ contact strength for wall-fluid repulsions (f_0^{rf})	1×10^{-12} N m^{-1}	set (Karunasena et al., 2014e)
LJ contact strength for wall-wall repulsions (f_0^{rw})	1×10^{-12} N m^{-1}	set (Karunasena et al., 2014e)
LJ contact strength for wall-fluid attractions (f_0^{a})	2×10^{-12} N m^{-1}	set (Karunasena et al., 2014e)
LJ contact strength for cell-cell repulsions (f_0^{rc})	1×10^{-10} N m^{-1}	set (Karunasena et al., 2014e)
Initial smoothing length (h_0)	$1.2 \times$ initial fluid grid spacing	set (Karunasena et al., 2014e)
Time step (Δt)	2×10^{-9} s	set (Karunasena et al., 2014e)

Table 3 Literature data used for qualitative and quantitative model validation

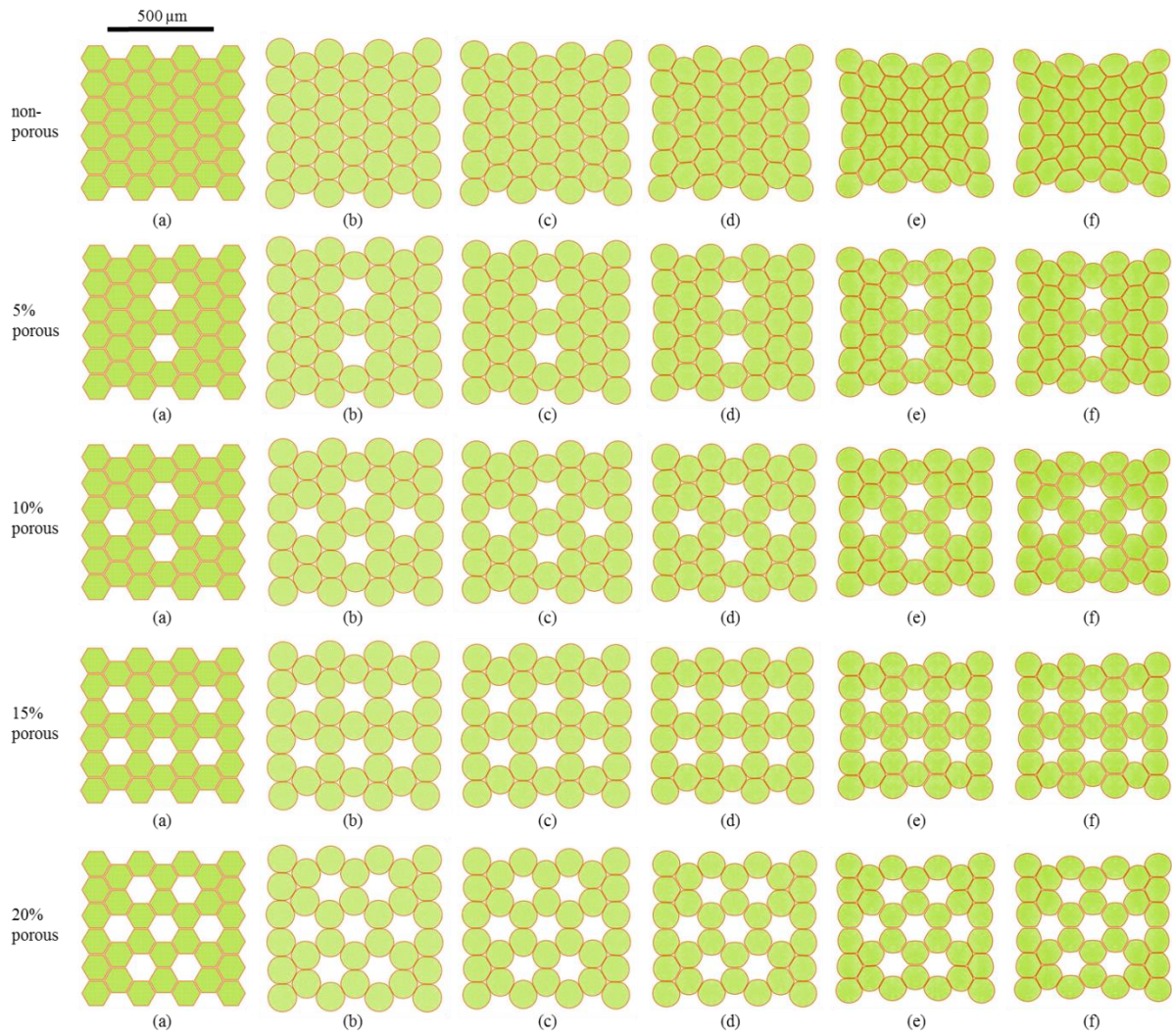| Plant variety	Qualitative data (microscopy images)	Quantitative data (A, D, P, R, EL and C)
Apple	(Karunasena et al., 2014a)	(Karunasena et al., 2014a; Mayor et al., 2005)
Grape	(Ramos et al., 2004)	(Ramos, 2010; Ramos et al., 2004)

Fig. 5. Simulation of porous apple tissues at different states of dryness: (a) initial condition before simulations, (b) $X/X_0 = 1.0$, (c) $X/X_0 = 0.8$, (d) $X/X_0 = 0.6$, (e) $X/X_0 = 0.4$, and (f) $X/X_0 = 0.3$.
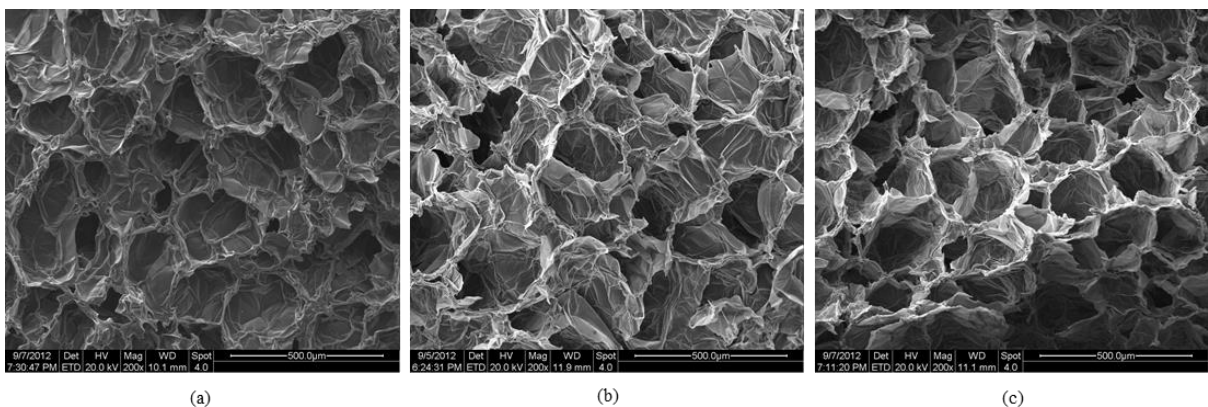

Fig. 6. Scanning Electron Microscopy (SEM) images of apple tissues at different states of dryness: (a) $X/X_0 = 1.0$, (b) $X/X_0 = 0.5$, and (c) $X/X_0 = 0.2$. (bar is 500 μm) (Karunasena et al., 2014a)
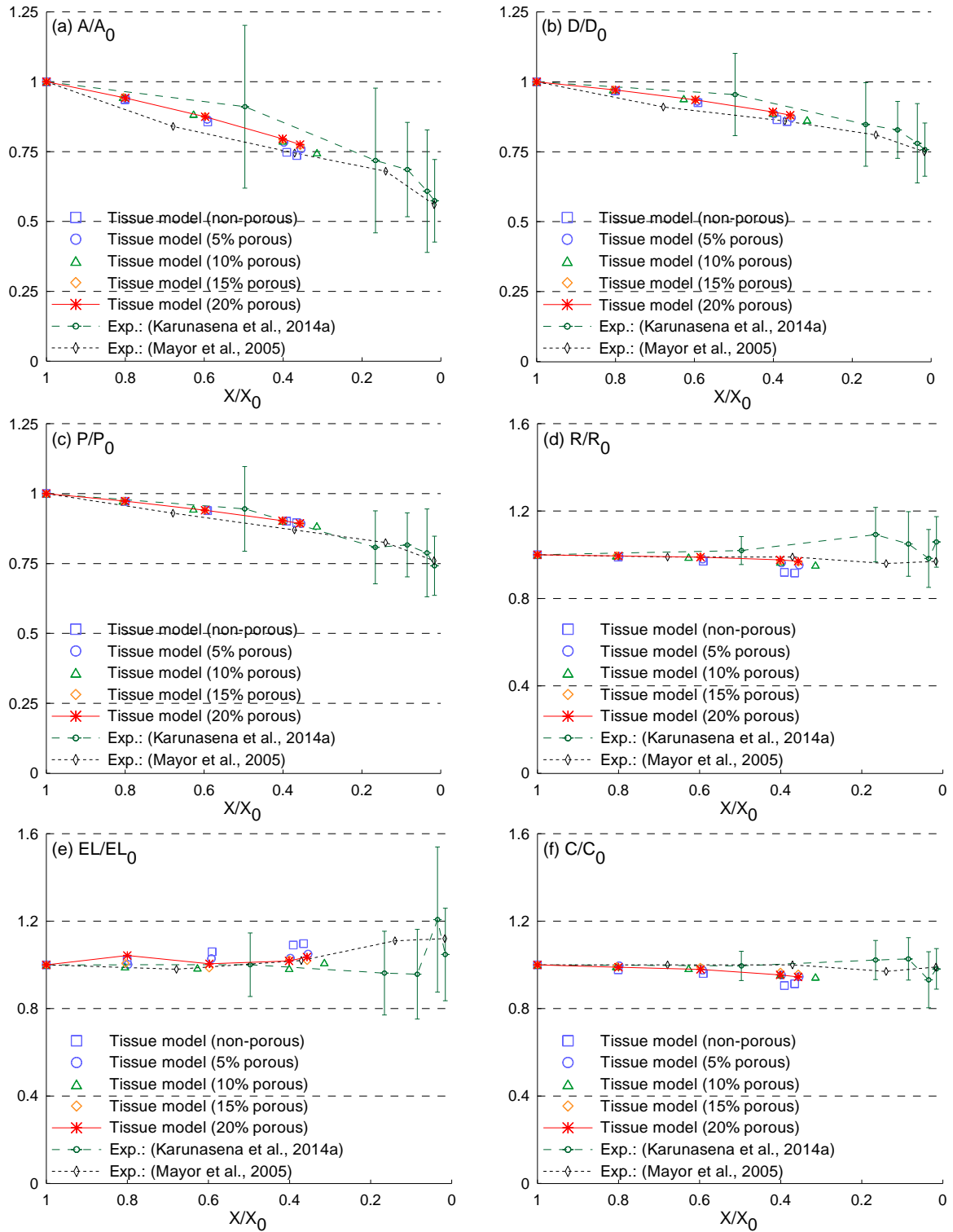
Fig. 7. Influence of porosity for cellular geometrical parameter variations of apple tissues during drying: (a) A/A_0, (b) D/D_0, (c) P/P_0, (d) R/R_0, (e) EL/EL_0, and (f) C/C_0.
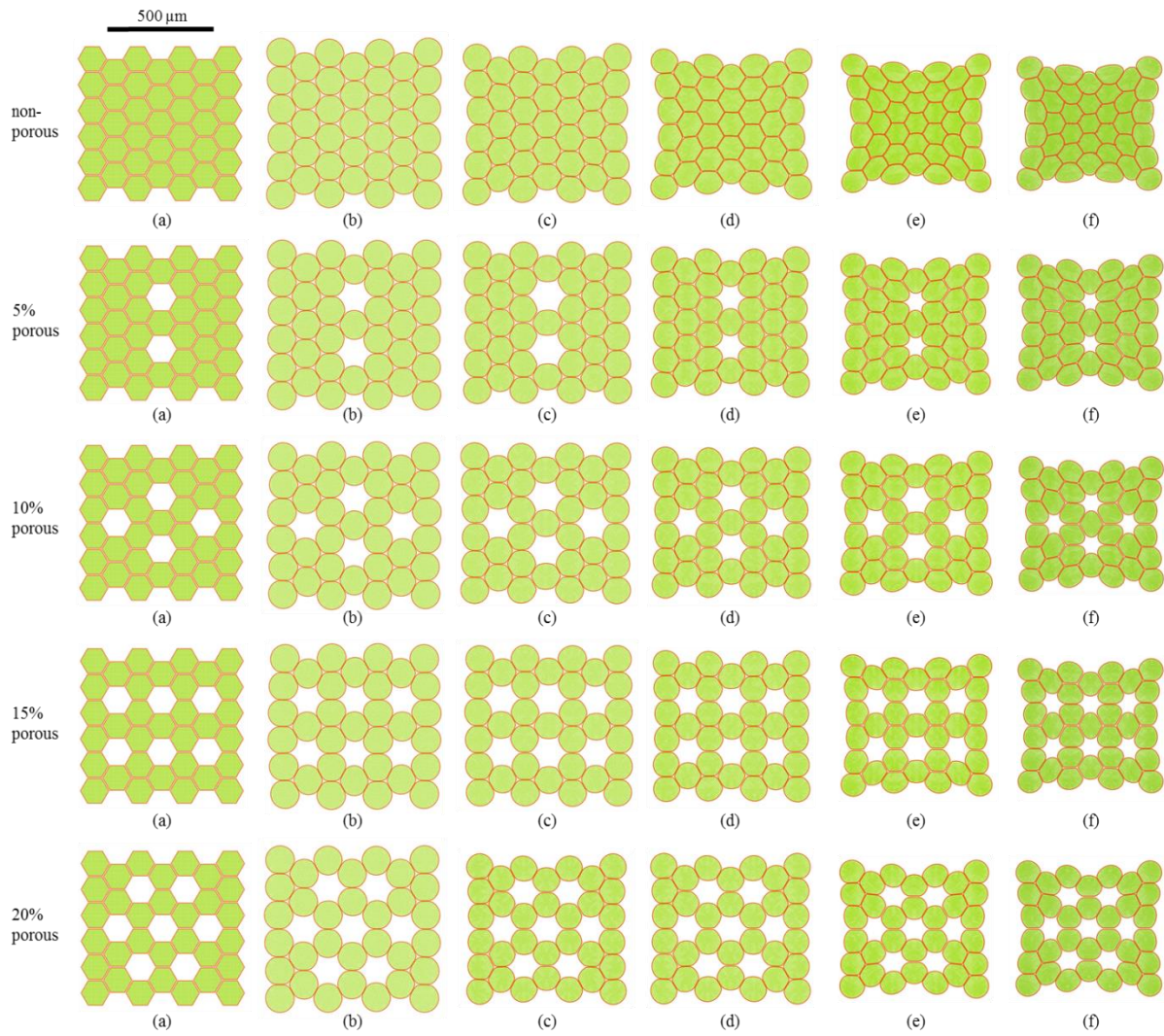
Fig. 8. Simulation of porous grape tissues at different states of dryness: (a) initial condition before simulations, (b) $X/X_0=$ 1.0, (c) $X/X_0 = 0.8$, (d) $X/X_0 = 0.6$, (e) $X/X_0 = 0.4$, and (f) $X/X_0 = 0.3$.
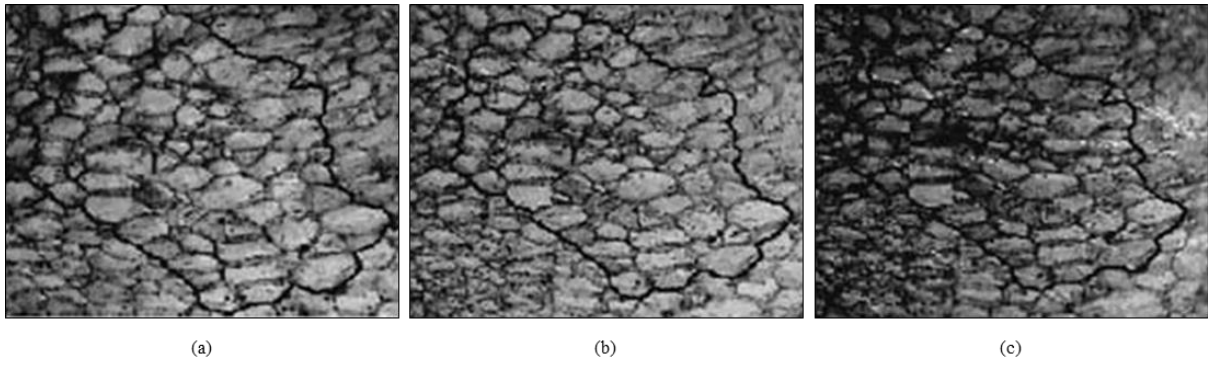
Fig. 9. Stereo microscopy images of grape tissues at different states of dryness[7]: (a) $X/X_0 = 1.0$, (b) $X/X_0 = 0.71$, and (c) $X/X_0 = 0.58$. (Ramos et al., 2004)

---

[7] "Reprinted from Journal of Food Engineering, 62(2), Inês N. Ramos, Cristina L.M. Silva, Alberto M. Sereno and José M. Aguilera, Quantification of microstructural changes during first stage air drying of grape tissue, 159-164, Copyright (2004), with permission from Elsevier"

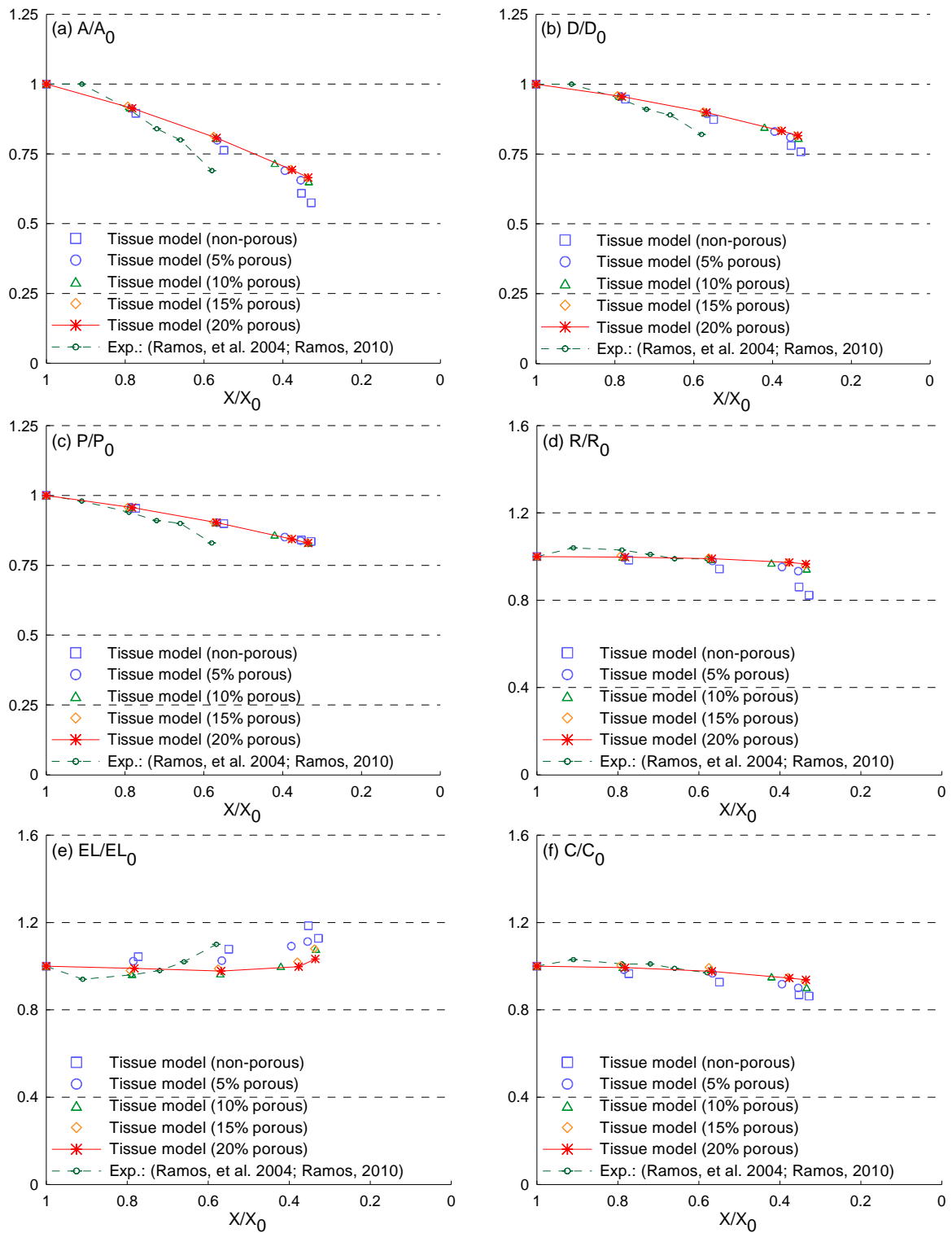Fig. 10. Influence of porosity for cellular geometrical parameter variations of grape tissues during drying: (a) A/A_0, (b) D/D_0, (c) P/P_0, (d) R/R_0, (e) EL/EL_0, and (f) C/C_0.
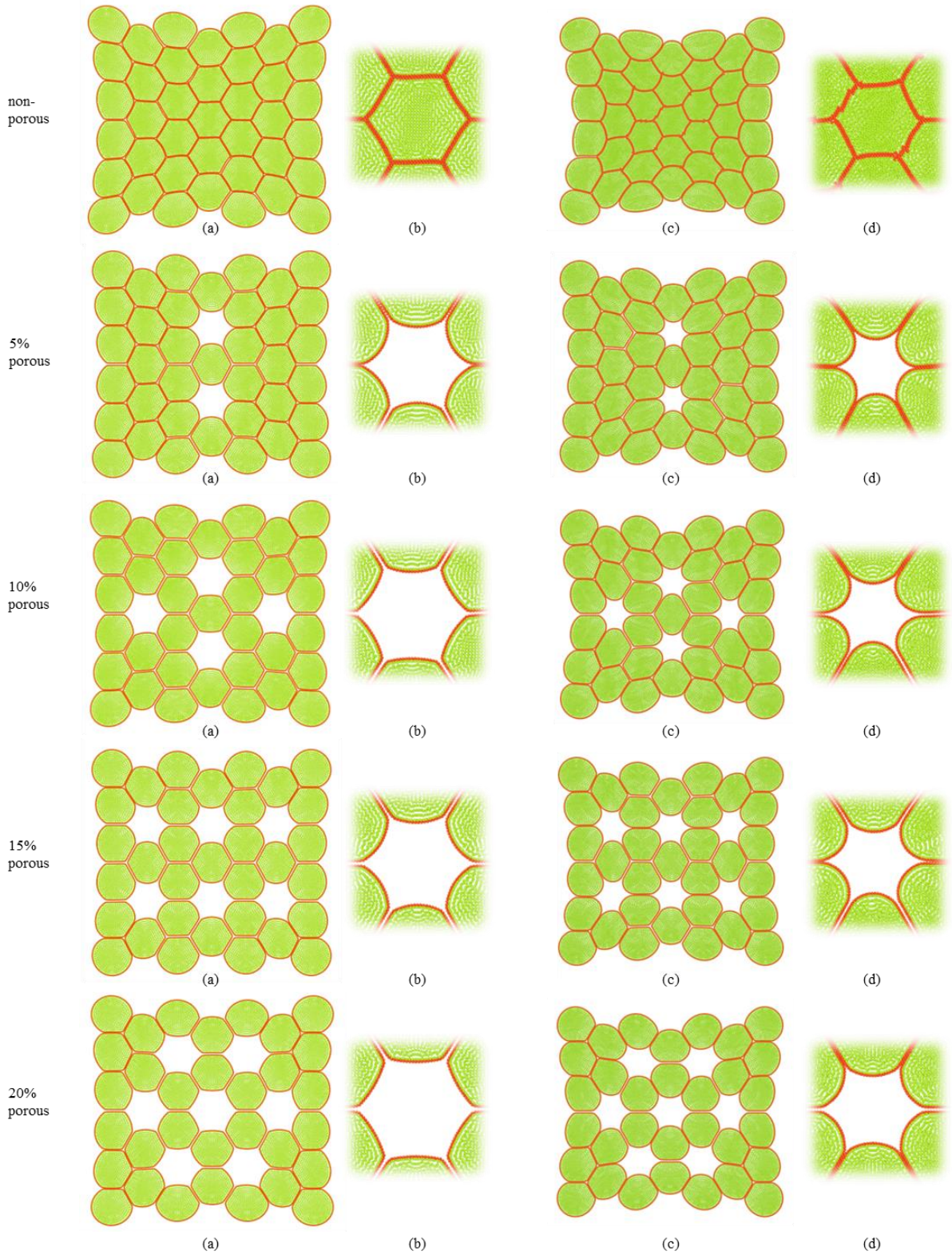
Fig. 11. Comparison of shrinkage of dried porous tissues at X/X_0 = 0.3: (a) apple tissue, (b) a cell/ pore of apple tissue (enlarged), (c) grape tissue, and (d) a cell/ pore of grape tissue (enlarged).
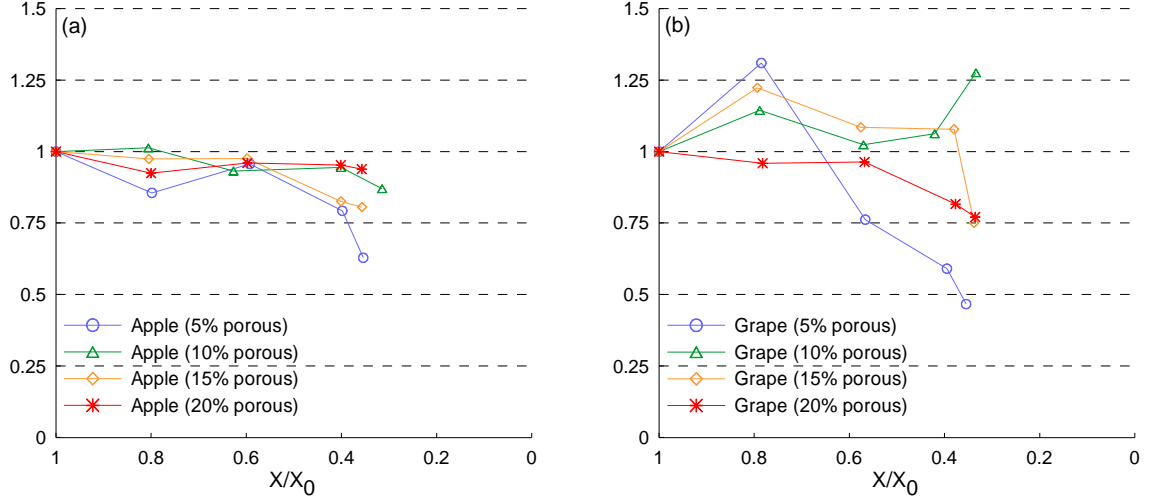
Fig. 12. Variation of porosity in different porous tissues during drying: (a) apple tissue, and (b) grape tissue.

9. Appendix A

9.1. Single cell model: DEM-based cell wall model

As mentioned in Section 2.1 and Figure 2, the total force ($\boldsymbol{F_k}$) on any wall particle k can be derived as:

$$\boldsymbol{F}_k = \boldsymbol{F}_{kj}^e + \boldsymbol{F}_{kj}^d + \boldsymbol{F}_{ki}^{rf} + \boldsymbol{F}_{kl}^{rw} + \boldsymbol{F}_{ki}^a + \boldsymbol{F}_{kj}^b + \boldsymbol{F}_{kj}^c. \tag{A.1}$$

Here, the $\boldsymbol{F}^e$ forces represent the cell wall resistance on extensions or contractions due to internal or external force interactions. Considering each wall element, a spring model is used to define the stiff forces $\boldsymbol{F}_{kj}^e$ on any wall particle k due to any bonded wall particle j as (Liedekerke et al., 2010):

$$\boldsymbol{F}_{kj}^e = GZ_0T_0\left(\lambda_\theta - \frac{1}{\alpha^2\lambda_\theta^5}\right), \tag{A.2}$$

where, G is the shear modulus ($\approx E/3$) with E being the Young's modulus of the wall material, Z_0 is the initial cell height, T_0 is the initial cell wall thickness, $\lambda_\theta = L/L_0$ is the extension ratio of any cell wall element at the current time step, L is the width of the wall element at the current time step (distance between particle k and j) and L_0 is its initial un-deformed width. The parameter α is calculated with $\beta = 0.5$ for cylindrical cells as follows (Liedekerke et al., 2010):

$$\alpha = \sqrt{\frac{\beta + \sqrt{\beta^2 - 4(\beta - 1)/\lambda_\theta^6}}{2}}. \tag{A.3}$$

25

In Eq. A.1, $\boldsymbol{F}^d$ forces represent the viscous behaviour of the fibrous cell wall boundary and are defined by using a linear dashpot model. Therefore the viscous forces $\boldsymbol{F}^d_{kj}$ acting on any wall particle k due to the neighbouring wall particles j are calculated as (Liedekerke et al., 2010):

$$\boldsymbol{F}^d_{kj} = -\gamma\, \boldsymbol{v}_{kj}, \tag{A.4}$$

where, γ is the cell wall damping constant and $\boldsymbol{v}_{kj}$ is the velocity of particle k relative to particle j. The $\boldsymbol{F}^{rf}$, $\boldsymbol{F}^{rw}$ and $\boldsymbol{F}^a$ forces in Eq. (A.1) were used to define the wall-fluid interactions and boundary conditions. The repulsion forces $\boldsymbol{F}^{rf}_{ki}$ on any wall particle k from any other fluid particle i are defined as (Liedekerke et al., 2010; G. R. Liu & Liu, 2003):

$$\boldsymbol{F}^{rf}_{ki} = f^{rf}_{ki}\, \boldsymbol{x}_{ki}, \tag{A.5}$$

where, f^{rf}_{ki} is the magnitude of the repulsion force and $\boldsymbol{x}_{ki}$ is the position vector of particle k relative to particle i. The f^{rf}_{ki} is defined according to Lenard-Jones (LJ) force type as (Liedekerke et al., 2010):

$$f^{rf}_{ki} = \begin{cases} f^{rf}_0\left[\left(\dfrac{\mathrm{r}_0}{\mathrm{r}_{ki}}\right)^8 - \left(\dfrac{\mathrm{r}_0}{\mathrm{r}_{ki}}\right)^4\right]\left(\dfrac{1}{\mathrm{r}_{ki}^2}\right) & \left(\dfrac{\mathrm{r}_0}{\mathrm{r}_{ki}}\right) \geq 1 \\[4mm] 0 & \left(\dfrac{\mathrm{r}_0}{\mathrm{r}_{ki}}\right) < 1, \end{cases} \tag{A.6}$$

where, r_0 is the initial gap between the two particles, r_{ki} is the current gap between them and f^{rf}_0 is the strength of the LJ contact. Furthermore, in Eq. A.1, in order to avoid unphysical self-penetrations of the non-bonded wall-wall particles, a similar force interaction was used to define the repulsion forces $\boldsymbol{F}^{rw}_{kl}$ with an LJ contact strength of f^{rw}_0. Also, the attraction forces $\boldsymbol{F}^a_{ki}$ were used to maintain fluid-wall contact during drying. Both interactions were modelled using LJ interactions with corresponding LJ contact strengths.

In Eq. A.1, a bending stiffness term ($\boldsymbol{F}^b_{kj}$) was used in order to account for the resistance that plant cell walls create when they experience local bending and wrinkling, and it was defined on any wall particle k within the k and j particle pair as (Karunasena et al., 2014b):

$$\boldsymbol{F}^b_{kj} = \frac{k_b}{L}\tan\left(\frac{\Delta\theta}{2}\right), \tag{A.7}$$

where, k_b is the cell wall bending stiffness, L is the width of any given wall element at any given time step, θ is the external angle between the particular wall element and the adjacent wall element as shown in Figure 2, and $\Delta\theta$ is the change of the θ angle during time evolution. Next, as given in Eq.

A.1, in order to account for cell wall contractions during drying, cell wall contraction forces ($\boldsymbol{F}^c$) were used in the model and are defined as (Karunasena et al., 2014c):

$$\boldsymbol{F}_{kj}^c = k_{wc} \left[L - L_0' \left[1 - \frac{a}{b}\left(1 - \frac{X}{X_0}\right) \right] \right],$$

(A.8)

where, k_{wc} is the force coefficient of wall contractions, L is the current width of any particular wall element (see Figure 1(d)), L_0' is the width of the wall element at fully turgid condition, a and b are empirical factors, and X/X_0 is the normalised moisture content of the dried cell to be simulated. The a and b were set by considering the normalised cell perimeter trends and the same k_{wc} was used for all food materials here (Karunasena et al., 2014c). Further, the cell wall drying effects were accounted by proportionally reducing the cell wall mass during drying (Karunasena et al., 2014c).

9.2. Single cell model: SPH-based cell fluid model

The resultant force $\boldsymbol{F}_i$ on any fluid particle i was defined as:

$$\boldsymbol{F}_i = \boldsymbol{F}_{ii'}^p + \boldsymbol{F}_{ii'}^v + \boldsymbol{F}_{ik}^{rw} + \boldsymbol{F}_{ik}^a .$$

(A.9)

In Eq. (A.9), the pressure forces ($\boldsymbol{F}_{ii'}^p$) and viscous forces ($\boldsymbol{F}_{ii'}^v$) on any given fluid particle i are defined using the generic SPH fundamental formulations by involving the properties of the neighbouring fluid particles i' as (Liedekerke et al., 2010):

$$\boldsymbol{F}_{ii'}^p = -m_i \sum_{i'} m_{i'} \left(\frac{P_i}{\rho_i^2} + \frac{P_{i'}}{\rho_{i'}^2} \right) \left(\frac{1}{Z} \right) \nabla_i W_{ii'},$$

(A.10)

$$\boldsymbol{F}_{ii'}^v = m_i \sum_{i'} \frac{m_{i'}(\mu_i + \mu_{i'})\boldsymbol{v}_{ii'}}{\rho_i \rho_{i'}} \left(\frac{1}{Z} \right) \left(\frac{1}{r_{ii'}} \frac{\partial W_{ii'}}{\partial r_{ii'}} \right),$$

(A.11)

where at any given time, m, P, ρ, μ, Z and W are the particle mass, pressure, density, dynamic viscosity, cell height and the smoothing kernel. For the smoothing kernel W, the quartic smoothing kernel was used for higher accuracy and stability rather than the commonly used cubic spline kernel (Karunasena et al., 2012d). When evaluating the W, the smoothing length was evolved in order to maintain approximately 20 particles within the influencing domain (Karunasena et al., 2014b) :

$$h = \left(\frac{D}{D_0} \right) h_0 ,$$

(A.12)

where, D is the average cell Feret diameter at the current time step, D_0 is the initial cell diameter and h_0 is the initial smoothing length (see Table 1 and Table 2). As the system evolves with time, the

following equation is used to update the fluid particle pressure as a function of slight fluid density variation (Liedekerke et al., 2010; G. R. Liu & Liu, 2003):

$$P_i = P_T + K \left[\left(\frac{\rho_i}{\rho_0} \right)^7 - 1 \right],$$
(A.13)

where, P_T is the uniquely set initial cell turgor pressure for each of the dried cell simulations (see Section 2.4.), K is the fluid compression modulus, ρ_i is the current density of each fluid particle, and ρ_0 is its initial density assumed to be equal to the density of water. Here, the K needs to be set sufficiently higher, in order to ensure the fluid behaves in a fairly incompressible manner within the SPH scheme by minimising large density fluctuations. Next, the density of any fluid particle i is evolved using the following equation (Liedekerke et al., 2010):

$$\frac{d\rho_i}{dt} = \frac{1}{Z} \frac{d\rho_i^*}{dt} - \frac{\rho_i^*}{Z^2} \frac{dZ}{dt} + \frac{\rho_i}{m_i} \frac{dm_i}{dt}.$$
(A.14)

The first term in Eq. (A.14) accounts for slight density changes of the cell fluid as the cell deforms in the XY plane and ρ_i^* is the 2-D density of any fluid particle i defined as $\rho_i^* = Z\rho_i$. Then the ρ_i^* fluctuations are defined using the standard SPH continuity equation as:

$$\frac{d\rho_i^*}{dt} = m_i \sum_{i'} \boldsymbol{v}_{ii'} \cdot \nabla_i W_{ii'}.$$
(A.15)

The second term in Eq. (A.14) adds a correction to the density evolution by compensating for any cell height changes, and is defined as:

$$\frac{dZ}{dt} = \frac{Z_{t+\Delta t} - Z_t}{\Delta t},$$
(A.16)

where, at any given time, $Z_{t+\Delta t}$ and Z_t are the cell heights at the current and previous time steps, and Δt is the time step size. Here, the cell height is time evolved by considering the incompressibility of the cell wall material as (Liedekerke et al., 2010):

$$Z = (\alpha \lambda_\theta) Z_0.$$
(A.17)

The third term in Eq. (A.14) accounts for the slight density changes within the SPH scheme as a result of the cell fluid mass transfer through the semi-permeable cell wall whenever there is a scalar difference between the cell fluid osmotic potential and the turgor pressure, and is defined as (Liedekerke et al., 2010; Taiz & Zeiger, 2010):

$$\frac{dm_i}{dt} = -\frac{A_c L_p \rho_i}{n_f} (P_i + \Pi),$$
(A.18)

where A_c, L_p, n_f and Π represent total surface area of the cylindrical cell at any given time, cell wall permeability assumed to be uniform all over the cell surface, total number of fluid particles used to model the cell fluid and the osmotic potential of the cell fluid at a given dried cell state, respectively.

The latter is carefully set to control the cell turgor pressure (Piotr P. Lewicki & Pawlak, 2003) because the amount of fluid transferred across the cell wall ceases when the value of P_i (> 0) becomes equal to the scalar value of Π.

The final two terms in Eq. (A.9) represent the fluid-wall boundary treatment which involves repulsion forces $\boldsymbol{F}_{ik}^{rw}$ and attraction forces $\boldsymbol{F}_{ik}^{a}$, and are defined in the same LJ force type as:

$$\boldsymbol{F}_{ik}^{rw} = \sum_k f_{ik}^{rw} \boldsymbol{x}_{ik} \,, \tag{A.19}$$

$$\boldsymbol{F}_{ik}^{a} = \sum_k f_{ik}^{a} \boldsymbol{x}_{ik} \,. \tag{A.20}$$

9.3. Tissue model

The pectin layer stiff force was defined as a linear spring model acting between the initially adjacent cell wall particles of any two adjacent cells, and defined as(Karunasena et al., 2014e):

$$\boldsymbol{F}_{km}^{e\_pectin} = -k_{pectin} \Delta \boldsymbol{x}_{km} \,, \tag{A.21}$$

where k_{pectin} is the pectin layer stiffness and $\Delta \boldsymbol{x}_{km}$ is the gap difference of the two particles compared to their initial gap. This force helps to maintain the gap between the wall particle pair equal to the initially set pectin layer thickness. Further, this is the only force acting in between cells if they try to separate each other beyond the initial pectin layer gap.

In the case where the interacting cells become closer, pectin stiffness creates a repulsion force in order to separate the cells and thereby tries to return them to their initial relative positions. The intensity of this force is usually insufficient to fully prevent the cells from becoming very close and eventually interpenetrated. Therefore, an LJ type force is used for this purpose, and is defined as (Karunasena et al., 2014e):

$$\boldsymbol{F}_{km}^{rc} = \sum_j f_{km}^{rc} \boldsymbol{x}_{km} \,, \tag{A.22}$$

where, f_{km}^{rc} is the strength of the LJ force field and $\boldsymbol{x}_{km}$ is the position vector of particle k relative to particle m. Here, the f_{km}^{rc} is defined as similar to that of the cell wall LJ force field.

9.4. Time evolution of the model

In the case of fresh tissue, each cell is set up by initiating the mass of the cell fluid and wall particles, and time-evolved by using the corresponding turgor pressure and osmotic potential values, thereby replicating real cells which have semipermeable cell walls. The cell fluid mass (i.e. mass of each fluid particle) tends to fluctuate until the turgor pressure and the magnitude of the osmotic potential become equal according to Eq. (A.18). Such fluid particle mass fluctuations result in fluid density fluctuation as defined by Eq. (A.14), which eventually causes sudden turgor pressure fluctuations as defined by Eq. (A.13). These turgor pressure fluctuations cause the cell wall to displace, leading to different states of cellular deformations. As a result, the turgor pressure fluctuates again, and it leads to secondary cell fluid mass fluctuations defined by Eq. (A.18). In the meantime, the cell wall mass is kept fixed at the initially set value, corresponding to the particular dryness state. This cycle of model evolution repeats until the cell turgor pressure becomes almost equal to the magnitude of the osmotic potential. At the end of the simulations, the steady state cell particle arrangement is referred to as the fresh cell state and the cell moisture content and other geometrical properties are computed to characterise the fresh cell state for analysis purposes (see Section 3 for details).

Dried tissues without case hardening are also similarly simulated and each cell in the tissue is initiated with identical model parameters and is time-evolved. Here, in order to conduct the simulations at minimum computational cost, a moisture content-based simulation approach is followed (Karunasena et al., 2014b). Also, as the cell moisture content reduces during drying, the turgor pressure is set to reduce in order to replicate actual plant cells during drying (Karunasena et al., 2014c). Furthermore, during drying, the moisture reduction from the cell wall and cell wall contraction effects are accounted (Karunasena et al., 2014c).